Heliyon 9 (2023) e21044

Contents lists available at ScienceDirect

Heliyon

journal homepage: www.cell.com/heliyon

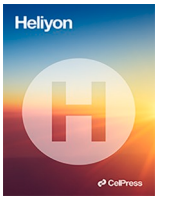

Geomorphological changes in young soils with sparse vegetation: Mathematical modeling and numerical simulation

Carlos Zambra [a,*], Benjamin Clausen [b], Diego Vasco [c], Roberto Lemus-Mondaca [d]

[a] Department of Industrial Technologies, Faculty of Engineering, University of Talca, Curicó, Chile
[b] Geocience Research Institute and Loma Linda University, Loma Linda, CA 92350, USA
[c] Department of Mechanical Engineering, University of Santiago, USACH, Av. Bernardo O'Higgins 3363, Santiago, Chile
[d] Department of Food Science and Chemical Technology, Faculty of Chemical and Pharmaceutical Sciences, University of Chile, Av. Dr. Carlos Lorca 964, Independencia, Santiago RM, Chile

ARTICLE INFO

Keywords:
Geomorphologic changes
Erosion numerical simulation
Particle transport
Mathematical modeling
Modeling rock weathering

ABSTRACT

This article presents an improved mathematical model and numerical simulation for weathering of large areas with complex topography. It uses the equations of momentum, temperature, and humidity in turbulent air and for heat and water infiltration into soils. A mathematical model is also presented to calculate the soil porosity fraction produced by physical rock weathering in areas where soil is produced from intrusive rocks (batholiths). An algorithm based on air velocity, humidity (rainfall), temperature variation, and soil topography was developed to quantify soil erosion and change of relief at each point and time step in air, at the ground surface, and within the soil. This results in a complete air-soil model based on conservation laws that have not previously been applied to large areas of the earth's surface. The mathematical model is solved using large-scale numerical simulations applied to an area of 6.6 km^2 in the Sierra Nevada batholith of California, USA. The results show that the wind velocity and resulting erosion is greater in areas with steeper slopes and that moisture accumulates mainly in low and flat areas; therefore, erosion is not uniform throughout the study area. In addition, computer simulations localized calculations to discrete grid cells within the porous (saprolite) fraction of the soil produced by freezing and thawing of water in rock. Results indicate that this physical mechanism is the primary contributor to weathering of rock at the study area.

1. Introduction

Soil erosion results from a combination of environmental factors such as temperature, wind velocity, environmental humidity, and precipitation, and geological factors such as soil type, porosity, particle size, etc. Disregarding tectonic movements, landslides, or water flooding, the erosion that changes the relief of a young soil under atmospheric conditions of high temperature variations and low rainfall can be summarized as a two-step process: first the soil formation and second the transport of soil particles by wind.

Weathering of intrusive rocks (batholiths) to soil is a long term process caused by a combination of basal rock weathering, structural development of the soil, and differentiation of that structure into horizons or layers [1]. Younger soils have physical and chemical characteristics similar to their parent, basal rock. Weathering results from a combination of volumetric strain due to

* Corresponding author.
E-mail address: czambra@utalca.cl (C. Zambra).

https://doi.org/10.1016/j.heliyon.2023.e21044
Received 14 July 2023; Received in revised form 11 October 2023; Accepted 13 October 2023
Available online 18 October 2023

humidity, precipitation, physical weathering by wind and temperature, and chemical weathering with mass loss due to chemical reactions produced mainly by water. Numerical simulations have been used to quantify the weathering of rock through chemical processes [2] in the laboratory [3] and in the field [4,5].

Freezing and thawing of water at the surface and inside the rock is one of the main physical agents for cracking and weathering rock. Although this is well known, it is common to study the weathering using only the bulk geochemistry of weathered rock [6] and to assume that volumetric strain from physical weathering is negligible [7]. Recent studies have shown that physical weathering should take priority in calculating rock weathering, since it is responsible for approximately 94 % of the variance in porosity fraction in subsurface soil [8]. This is especially relevant if there is high humidity and temperature variations [6,9]. In order to incorporate these natural mechanisms in this work, we incorporated wind velocity, humidity, and temperature of air passing over the soil surface that wets the rock and soil by water infiltration and produces stress and strain. We were unable to find past numerical simulations that coupled long-term water infiltration and temperature in soil and its surface relief with turbulent fluid dynamic, temperature and air humidity (rainfall) over the ground surface. A significant characteristic of the study proposed here simplifies the mathematical model by considering soil production only through physical weathering. To simplify the model and simulations the effects of chemical weathering are neglected.

Particles produced by weathering are available for wind transport which is an effective agent for weathering and transporting significant amounts of sand and bedrock. Studies using techniques such as cosmogenic ^{10}Be [10,11] and luminescence profiles [12] have been used successfully to relate erosion and wind. Surfaces in contact with wind are very sensitive to it, especially at depths of 2–3 cm [13]. The dryness or saturation of water on the surface may be directly related to wind erosion of a soil or weathering of a rock. Bonds between grains are stronger when humidity increases and vary in different soil types with the same humidity content [13]. This makes it necessary to incorporate the calculation of humidity to improve the approximations of weathering and erosion.

An extensive review of articles published on erosion modeling between 1994 and 2017 found that 94 % are based on erosion only by water while 0.9 % include the combination of water and wind [14]. The same study observed that the vast majority of models (e.g. USLE family models, GASEMET, or BQART models) simulate processes of sheet and rill delivery of fluvial sediments, soil displacement due to water, tillage operations, and land vulnerability due to wind erosion [14]. These models are mainly based on global erosion rates and average precipitation and provide good results when compared to complex natural processes, mainly in humid climates. Such models generally use data about erosion rates, precipitation and, less frequently, wind velocity in empirical equations or statistical probabilities. These models do not include a calculation of soil formation due to rock weathering or the local air velocity, humidity, and temperature changes on the ground; therefore, they are not accurate enough in areas with exposed igneous rocks, young soil on batholiths with little or no vegetation, or sudden changes in wind velocity due to abrupt changes in relief.

This paper simulates the atmospheric boundary layer (ABL) on the ground by using the standard $\kappa-\varepsilon$ turbulence model. This two-equation model that calculates the turbulent stress in the Reynolds-averaged Navier-Stokes (RANS) equations is one of the most frequently used, mainly because of its numerical stability and low computational cost [15]. This model has been shown to work well for external flows around bluff bodies [16]. The $\kappa-\varepsilon$ model has recently been used to simulate ABL over complex areas [15], buildings [17], and wind farms [18]. The transport of particles from a fixed source depends on a certain threshold wind velocity of the ABL, moisture of the ABL, and particle size [19,20]. In our simulations, calculation of wind velocity for the ABL takes into account ground relief, humidity, and temperature, which allows us to estimate the local variation of the wind velocity with better precision. Since the study of soil erosion is very relevant to the evolution of natural ecosystems and to human activities, it is worthwhile to develop tools that incorporate as many environmental variables and the interactions between them as possible in order to improve the accuracy of the results. The goal of this work is develop a mathematical model and simulations to estimate the soil erosion incorporating the calculations of wind velocity, humidity and temperature in the air and soil and their interaction with the local relief. In brief, this paper proposes a tri-dimensional mathematical model to calculate soil erosion due to coupled effects from turbulent wind velocity, humidity, and air temperature in relation to the soil surface temperature, water infiltration, and complex surface geometries. The mathematical model is solved using the finite volume method with our own programmed codes. Values from our numerical simulations are used to calculate the threshold velocity, the humidity of soil, and the physical weathering by freezing and thawing. Resulting changes in relief 150 ka forward and 150 ka back in time are presented. This study is limited to the calculation of erosion in young soils from intrusive rock weathering with sparse vegetation on its surface. This model does not consider erosion as a result of landslides, water channeling, or soil displacement due to water, nor abrupt changes in relief due to geological processes, such as plate tectonic displacement. Outside of these limitations, the mathematical model and the computational code can be used for any geographic area.

This paper is organized as follows: Section 2 presents the background for the area where the study was applied. Section 3 describes a mathematical model for air and soil, the initial and boundary conditions, and equations for calculating physical rock weathering and soil erosion. Section 3 also outlines the numerical procedure to solve the governing equations and the algorithm developed for determining change in relief of the ground surface. In section 4, our model is solved for rock erosion in a wind tunnel and validated by comparing numerical results with experimental ones and carrying out a grid sensitivity study. Finally, the algorithm is applied to the Fine Gold area in the Sierra Nevada Mountains of California.

2. Simulation for Fine Gold

To investigate the ability to predict erosion in soils produced from weathered rocks, this paper considers an area in the Sierra Nevada Batholith of northern California called the “Fine Gold intrusive complex”. This location was chosen because it is a well-studied area. More than ten years of field data is available from the nearby meteorological station at Millerton Lake. Other data from experimental studies include erosion rate, mass transfer coefficient and volumetric strain, all of which are needed for incorporation

into the simulations. Fig. 1a shows a satellite image with the GPX (GPS exchange format) coordinates of the study area marked with dashed white lines. The extraction site of material used to obtain erosion rate (*ER*) and bulk mass transfer coefficient (τm) [8] is marked with a pin. The relief data were obtained from Google Earth © and transferred to a map shown in Fig. 1b which was made using free QGIS © software. An inlet from Millerton Lake shown in the southwest corner used no special equations to model erosion for the simulations. The elevations in the study zone vary from 180 to 480 m above sea level (masl), some of the lowest of the Sierra Nevada Batholith. Vegetation is sparse, but rock outcrops are uncommon because weathering of the bedrock tonalite to saprolite has produced the present-day soil covering the area [21]. The area was not glaciated in the Pleistocene [22].

Table 1 lists the average monthly temperature (T_{avg}), wind velocity (U_{avg}), monthly average of days with precipitation (*MADP*), and relative humidity (RH) from ten years of data at the Millerton Lake meteorological station [23]. The mathematical model uses these values as boundary conditions.

The erosion rate (*ER*), average annual precipitation (*AAP*), and mass transfer coefficient (τm) for weathered rock in the study area are 0.03 mm/yr, 473 mm/yr, and −0.1, respectively [8].

3. Mathematical model

A complex mathematical model results from considering the large number of variables that can affect soil erosion due to physical causes, e.g., temperatures, humidity, air velocity, properties of soil, infiltration, etc. This section presents the mathematical model developed and programmed for the simulations. Due to the extensive set of equations that are solved, a summary of the main characteristics of the mathematical model is presented here while all the set of equations are detailed in the supplementary material. This includes the main physical variables that influence the weathering of the rock and the formation of the soil and compares the calculated turbulent velocities over the ground with the threshold velocity needed to carry particles.

3.1. Mathematical model for turbulent air, temperature, and humidity over soil

Our mathematical model was based on the conservation law for incompressible turbulent flow of momentum in three dimensions (x,y,z). The effects of turbulence are included by the usual decomposition of each transport variable into the sum of a statistical mean value plus turbulent fluctuations, followed by averaging of the corresponding RANS transport equations. The airflow is modeled using variable density, but is quasi-incompressible, i.e., the low-Mach number approximation; thus, density changes are associated with temperature variations, but are not directly coupled with pressure. The governing equations for the average air flow include the mass conservation (or continuity) equation and the conservation equation for linear momentum.

$$\frac{\partial \overline{\rho}}{\partial t} + \nabla \cdot (\overline{\rho}\,\overline{\mathbf{u}}) = 0 \tag{1}$$

and the conservation equation for linear momentum

$$\frac{\partial (\overline{\rho}\,\overline{\mathbf{u}})}{\partial t} + \nabla \cdot (\overline{\rho}\,\overline{\mathbf{u}}\,\overline{\mathbf{u}}) = -\nabla p + \nabla \cdot \left[(\mu_a + \mu_t)\left(\nabla \overline{\mathbf{u}} + \nabla \overline{\mathbf{u}}^T\right)\right] + \overline{\rho}\mathbf{g} \tag{2}$$

The overbars denote mean values, with $\mathbf{u}$ as the flow velocity vector field, p as the pressure, $\mathbf{g}$ as the gravitational acceleration, μ_a as the dynamic viscosity of air and μ_t as the local turbulent viscosity. This last variable is introduced as a closure for the turbulent stresses arising from the velocity decomposition. The isotropic part of the turbulent stress tensor has been absorbed into the pressure term.

Mass conservation and linear momentum equations are coupled with the thermal energy and moisture content equation in the air.

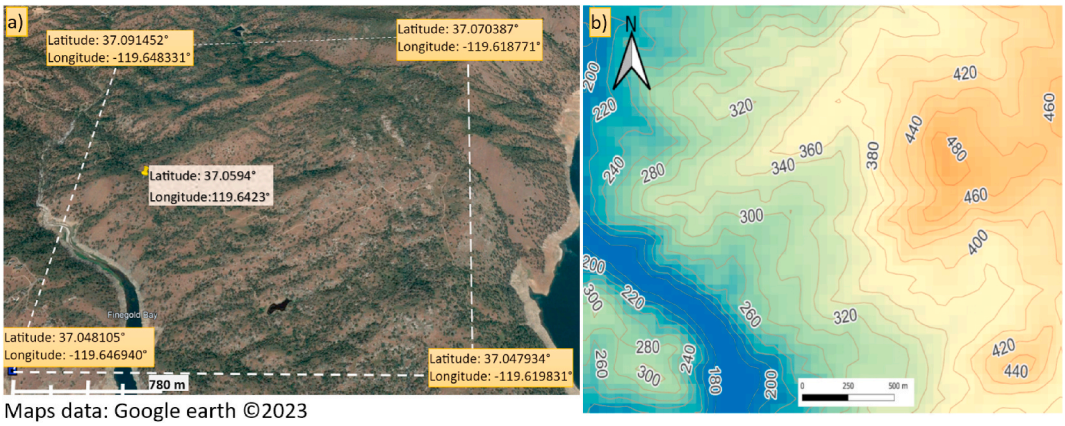

Fig. 1. The Fine Gold study area in the foothills of the Sierra Nevada Mountains, California, USA: a) satellite image with the quadrilateral dashed white line outlining the study area and the sampling point labeled and b) topographic map showing relief within the dashed white line. (For interpretation of the references to color in this figure legend, the reader is referred to the Web version of this article.)

Table 1
Average atmospheric conditions at Millerton Lake in the Fine Gold study area.

	Jan	Feb	Mar	Apr	May	June	July	Aug	Sept	Oct	Nov	Dec
T_{avg} (°C)	10	11	13	17	21	26	30	30	28	20	14	10
U_{avg} (m s^{-1})	1.7	1.9	2.2	2.5	2.5	2.5	2.2	2.2	1.9	1.7	1.7	1.7
MADP	5	4	5	2	1	1	0	0	0	1	3	5
RH (%)	63	62	60	53	43	32	27	27	30	38	50	62

The energy equation, expressed using temperature as the dependent variable, is

$$\frac{\partial(\overline{\rho}\,\overline{T})}{\partial t}+\nabla\cdot(\overline{\rho}\,\overline{\mathbf{u}}\,\overline{T})=\nabla\cdot\left[\left(\overline{\rho}\alpha_{air}+\frac{\mu_t}{\mathrm{Pr}_t}\right)\nabla\overline{T}\right] \tag{3}$$

where α_{air} is the thermal diffusivity and Pr_t is a turbulent Prandtl number applied as a closure for the turbulent heat diffusion. For the transport equation of moisture content in the air ($\overline{\theta}_{w,air}$) we have a similar equation

$$\frac{\partial(\overline{\rho}\,\overline{\theta}_{w,air})}{\partial t}+\nabla\cdot(\overline{\rho}\,\overline{\mathbf{u}}\;\overline{\theta}_{w,air})=\nabla\cdot\left[\left(\overline{\rho}D_{w,a}+\frac{\mu_t}{\mathrm{Sc}_t}\right)\nabla\overline{\theta}_{w,air}\right] \tag{4}$$

where $D_{w,a}$ is the molecular mass diffusivity of water vapor in air and Sc_t is a turbulent Schmidt to account for the turbulent mass diffusion. We define the water content to be the volumetric ratio of water in air, i.e., volume of water divided by total volume of air.

The turbulent viscosity is computed by applying the κ–ε turbulence model, which consists of an equation for the turbulent kinetic energy κ,

$$\frac{\partial(\overline{\rho}\kappa)}{\partial t}+\nabla\cdot(\overline{\rho}\,\overline{\mathbf{u}}\,\kappa)=\nabla\cdot\left[\left(\mu_a+\frac{\mu_t}{\sigma_\kappa}\right)\nabla\kappa\right]+G-\overline{\rho}\varepsilon \tag{5}$$

and an equation for the turbulent kinetic energy dissipation rate ε,

$$\frac{\partial(\overline{\rho}\varepsilon)}{\partial t}+\nabla\cdot(\overline{\rho}\,\overline{\mathbf{u}}\,\varepsilon)=\nabla\cdot\left[\left(\mu_a+\frac{\mu_t}{\sigma_\varepsilon}\right)\nabla\kappa\right]+GC_1\left(\frac{\varepsilon}{\kappa}\right)-\overline{\rho}C_2\left(\frac{\varepsilon^2}{\kappa}\right) \tag{6}$$

Classical wall functions for the standard $\kappa-\varepsilon$ turbulence model were applied to the flow conditions in the cells adjacent to the cell walls or in the rock [24]. These functions are based on the law-of-the-wall region of the boundary layers; whereas the $\kappa-\varepsilon$ model takes control farther from the surface and in the free stream region. Additional explanation of the κ–ε turbulence model and wall functions for velocity and temperature used in our computer code may be found in Ref. [25] and supplementary material of this paper.

3.2. Mathematical model for diffusion of temperature and humidity in rock and soil

The transport phenomena within the rock and soil is treated as conjugate with the processes in the surrounding air. For simplicity, a local thermal equilibrium is assumed between the solid and fluid inside the porous rock or soil. In the Fine Gold study area of California, the solid rock and weathered soil have the geochemical composition of tonalite. Granodiorite and tonalite have a similar chemical composition [26], so we consider that the thermal diffusivity of granodiorite can be used for both. Below a depth of 30 m all the tonalite rock is considered to be fresh; therefore, porosity is near zero and we use the thermal diffusivity of granodiorite for the soil.

To quantify water flow in the soil, volumetric water content is used and defined as the volume of water in soil per total volume of soil. The simulation of water infiltration in soil used a 3D unsteady equation for water content (θ) in unsaturated porous material obtained from the Darcy-Buckingham law and the mass conservation [27].

More details of the equations and parameters used in this section can be found in the supplementary material of this paper.

3.3. Initial and boundary conditions

Modeling was carried out for neutral atmospheric stability in a transient state. Due to these conditions, mechanical turbulence predominates. Velocity variables are initially set to zero. The air enters from the *y,z* (at x=0) or *x,y* (at z=0) planes with a southwest wind direction. This boundary condition is adopted because it is the predominant wind direction for the Fine Gold study location [23]. For these input planes, a velocity profile based on the average wind velocity $U_{in}\ (m/s)$ uses an exponent $p=0.14$ that corresponds to a neutral atmosphere. The velocities in the u and w directions in the x=0 and y=0 planes take into consideration the irregular air-soil surface and are calculated as follows:

$$\begin{aligned} u_{in}(0,y,z,t)&=U_{avg}\left(\frac{(y_{x=0,air})}{10}\right)^p\cdot\cos(45);\quad u_{in}(x,y,0,t)=U_{avg}\left(\frac{(y_{z=0,air})}{10}\right)^p\cdot\cos(45)\\ w_{in}(0,y,z,t)&=U_{avg}\left(\frac{(y_{x=0,air})}{10}\right)^p\cdot\sin(45);\quad w_{in}(x,y,0,t)=U_{avg}\left(\frac{(y_{z=0,air})}{10}\right)^p\cdot\sin(45)\end{aligned} \tag{7}$$

Symmetry at planes $x=x_{max}$, $y=y_{max}$ and $z=z_{max}$ (see Fig. 2) are imposed for u, v and w velocities and temperatures (T).

The air temperature in the study area is initially set at 20 °C or 293 K. In the soil, a linear temperature gradient of 25 K per kilometer (0.025 K/m) of depth starting with 293 K at the surface was imposed at time 0 using the follow equation:

$$T(x_{soil}, y_{soil}, z_{air}, 0) = 0.025 \cdot y_{soil} + 293 \tag{8}$$

This gradient is commonly used in the literature for heat flow from the Earth's mantle [28].

The air temperature in the study area was varied according to the monthly average measurements, $T_{in}(0, y_{air}, z_{air}, t) = T_{avg}$. The values of T_{avg} for the study area are listed in Table 1.

The water content in unsaturated soil and weathered rock varies with the depth. The water content varies between $\theta_w(x, y_{soil} = 0, z) = 0.2$ at the surface and $\theta_w(x, y_{soil} = -30m, z) = 0.01$ at 30 m of depth. An initial non-linear polynomial equation was arbitrarily implemented to simulate this initial unsaturated water condition of the weathered soil:

$$\theta_w(x, y_{soil} = 0m - 30m, z, 0) = -1.69 \times 10^{-5} \cdot y_{soil}^3 + 6.65 \times 10^{-4} \cdot y_{soil}^2 - 1.14 \times 10^{-2} \cdot y_{soil} + 2.04 \times 10^{-1} \tag{9}$$

Below 30 m depth, an average water content of 0.01 is assumed for fresh granodiorite rock [29]. An initial 1 % water content of air is used for the moisture value at $\theta_{w-air}(x_{air}, y_{air}, z_{air}, 0) = 0.01$. The moisture content of air entering the study area ($\theta_{w-air,in}$) is calculated by assuming an ideal gas mixture that depends on temperature (T_{in}, K) and relative humidity (RH, %):

$$\theta_{w-air,in}(0, y_{air}, z_{air}, t) = \frac{RH \cdot p_{va}^*}{RT_{in} \cdot \rho_{w,va} \cdot 100} \tag{10}$$

In this equation R is the ideal gas constant (461.5 J K^{-1} kg^{-1}), $\rho_{w,va}$ is the density of moist air, and p_{va}^* represents the saturated vapor pressure (in Pascals) that is calculated as follows:

$$p_{va}^* = 0.114 \cdot T^3 - 3.33 \cdot T^2 + 121 \cdot T + 340 \tag{11}$$

Rain was incorporated as a boundary condition by considering the relative humidity (RH) as equal to 1 during the monthly average of days with precipitation ($MADP$) reported in the study area (see Table 1).

3.4. Weathering of a fresh rock and erosion of the soil

Since it is assumed that weathering is produced mainly by the physical variables humidity, precipitation, wind velocity, and temperature, only the equations to quantify physical weathering will be taken account. To develop the weathering model, we assume that erosion of rocks occurs in two steps: soil production by weathering of the rock surface and dragging of the weathered soil material by the wind. Stress on the surface of the rock ($S_{r,w}$) and total strain (εr_{sum}) are related by the elastic Young's modulus (σ_r) which can be used to calculate the strain due to wind striking a rock:

$$\varepsilon r_{ph,w} = \frac{S_{r,w}}{\sigma_r} = \frac{\frac{F_w}{A_r}}{\sigma_r} = \frac{F_w}{\sigma_r \cdot A_r} \tag{12}$$

where F_w is the force of the wind and A_r is the surface area of the rock. The wind force depends on the resultant wind velocity ($v_{w,res}$) which in this paper is calculated using the momentum equations. Young's modulus depends strongly on moisture. An equation obtained experimentally [13] is used to relate the humidity of the rock (WL(%)) and the Young's modulus.

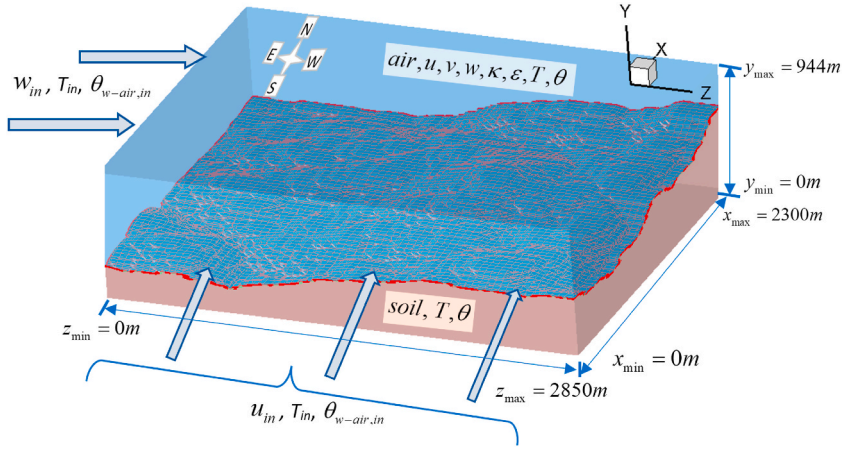

Fig. 2. Diagram of the 3D computational domain including physical parameters used in the simulation.

$$\sigma_r(WL(\%)) = 1E-3 \cdot \left(\frac{WL(\%)}{2E7}\right)^{\frac{1}{-2.345}} \tag{13}$$

A rock surface is deformed by the action of moist wind, by chemical reactions, and by expansion and contraction due to freezing and thawing of the water it contains. The rock expands or contracts in response to the total strain εr_{sum} on it. Water on the rock surface can be directly related to the moisture in the air and precipitation; therefore, the deformation or strain of the rock is directly related to its chemical and physical weathering. The total or volumetric strain (εr_{sum}) on a rock is defined as the change in volume (V) as a fraction of the initial volume of the rock:

$$\varepsilon r_{sum} = \varepsilon r_{ph} + \varepsilon r_{ch} = \frac{V_{wtr} - V_{prt}}{V_{prt}} = \frac{V_{wtr}}{V_{prt}} - 1;\ \varepsilon r_{ph} = \varepsilon r_{ph,w} + \varepsilon r_{ph,AAP} \tag{14}$$

The subscripts *prt* and *wtr* refer to the protolith or initial state of the rock and the weathered rock or saprolite volume of soil, respectively. The total strain is the sum of the physical (εr_{ph}) and chemical (ε_{ch}) strain.

The total strain can be calculated from field data such as the porosity of the soil (ψ_{wtr}) and the mass transfer coefficient (τm) using the follow equation proposed by Ref. [8]:

$$\varepsilon r_{sum} = \frac{-(\tau m + 1)}{\psi_{wtr} - 1} - 1 \tag{15}$$

The fraction of porosity, F_{PP}, produced by strain from physical weathering can use to find the porosity of the soil [8].

$$\psi_{wtr} = \frac{\tau m}{(F_{PP} - 1)} \tag{16}$$

A linear regression model based on field data for erosion rate (*ER, mm/yr*) and average annual precipitation (*AAP, mm/yr*) was proposed [8] to find the value of F_{PP}.

$$F_{PP} = 2.6 + 5.1 \cdot ER - 0.74 \cdot \log_{10} AAP \tag{17}$$

Substituting F_{PP} in Eq. (16) and ψ_{wtr} in Eq. (15) and assuming a constant value for τm, the total volumetric strain (εr_{sum}) is calculated.

If strain on the rock due to chemical weathering is neglected ($\varepsilon r_{ch} = 0$), strain due to physical weathering is equal to the total strain ($\varepsilon r_{sum} = \varepsilon r_{ph}$). Then strain due to contraction and expansion of water around and inside the rock can be calculated by rearranging Eq. (14) as follows:

$$\varepsilon r_{ph,AAP} = \varepsilon r_{ph} - \varepsilon r_{ph,w} \tag{18}$$

The second and final stage of the erosion process is transport of the weathered material away from its source location. In this work, transport by floods is disregarded, so we model wind as the only external force causing transport. A minimum wind velocity ($U_{th,m}$) is necessary for this. The following equation obtained experimentally for moistened sand of diameter less than 0.01 cm is used to calculate the threshold wind velocity (m s^{-1}) necessary for transport of the weathered material [20],

$$U_{th,m} = \left((38.52 - 1265.4 \cdot d)\left(1 + K_{fg} M\right)^{1/2}\right) \Big/ 100, d < 0.01\ \ cm \tag{19}$$

where M is the gravimetric water content (% *w/w*), K_{fg} is a correction factor (2 in this paper) related to grain size, and d is the sand grain diameter (cm).

Additional details of the equations used in this section can be found in the supplementary material. The mathematical model outlined in previous sections is solved in a coupled way according to the computational procedure described below.

4. Numerical procedure

The mathematical model described above is solved using the finite volume method (FVM) [30,31]. The computational domain is discretized with a non-regular grid built with rectangular parallelepipeds. The development of the numerical simulation is based on a non-commercial computer code written in FORTRAN, which has been fully validated in several published works [32,33]. In the FVM, the governing equations are treated in the generalized form for the transport of a variable φ, with unsteady convection, diffusion, and source terms (S_c, S_p):

$$\frac{\partial(\overline{\rho}\varphi)}{\partial t} + \nabla \cdot (\overline{\rho}\ \overline{\mathbf{u}}\ \varphi) = \nabla \cdot (\Gamma \nabla \varphi) + S_c + S_p \varphi \tag{20}$$

which are integrated in the finite volume cells.

In this formulation, processes in the air flow and the rock are treated as a conjugate problem. Thus, for cells occupied by rock and soil, the velocity vector $\overline{\mathbf{u}}$ vanishes and heat and mass diffusion become the only transport mechanisms. The algorithm includes internal (at each iteration) and external iterations (at each time step). The governing equations are coupled sequentially in the internal iteration with the SIMPLE algorithm [25]. Under-relaxation coefficients are applied to these internal iterations using a value of 0.5 for all the variables, except for the pressure correction which uses a value of 0.9 instead. The discretized equations for each dependent variable φ

are solved iteratively for the internal iterations with a line Gauss-Seidel method combined with a Tridiagonal Matrix Algorithm (TDMA).

The convergence criterion for the internal iteration was a maximum difference of 1×10^{-4} between successive solutions at any control volume for all variables. The time (t) integration is calculated with an implicit Euler scheme. A residual of the continuity equation less than or equal to 1×10^{-3} was used as the convergence criterion for the time step in the external iteration. The resulting algorithm uses a semi-implicit scheme for pressure-linked equations. The stability of this scheme is high and good results are generally obtained, which is why it is used by commercial programs such as Ansys-Fluent. However, if adequate convergence criteria are not adopted, it is not possible to ensure adequate results. The convergence criteria used in this study have been used to simulate heap leach and bioleaching over large plots of land and have proven to be adequate [33]. In addition, to ensure the precision of the results, the developed algorithm was subjected to a mesh study and comparisons with experimental results (see section 5). A detailed explanation of the FVM used here can be found in Ref. [25]. The resulting algorithm can be downloaded from the following link (https://drive.google.com/drive/folders/1kqiNYx9QtUxGnTlrze5m18a0QQm_x5VA?usp=share_link) and is explained step by step in the supplementary material for this article.

4.1. Simulation conditions for the Fine Gold area

The programmed algorithm includes a subroutine to fit the latitude, longitude and altitude relief data to the computational grid. The atmospheric boundary layer (ABL) near ground level is defined as the lowest part of the troposphere directly affected by the earth's surface; its thickness can vary from hundreds of meters to more than a thousand meters vertically [34]. Turbulent flow caused by terrain relief occur in this area.

For this study, the ABL was included by arbitrarily multiplying the maximum ground altitude $y_{soil} = 480$ m by a factor of 1.966. The resulting domain for calculations was 2300 m, 944 m, and 2850 m in the *x, y,* and z directions. A non-uniform grid with 126x175x132 nodes in the *x, y,* and *z* directions was used for simulations, with the 2910600 control volumes being denser in areas just above the soil-air ground surface. This results in control volumes of 2.86 m in the *y*-direction at the soil-air interface. The computational control domain with the surface grid is shown in Fig. 2. This figure also displays the variables for air and soil used in the algorithm.

Simulations were carried out for two cases: 150 ka forward in time and 150 ka back in time.

4.2. Numerical procedure to change the volume of soil due to erosion

This section explains the computational procedure used to introduce a volume change in the soil surface by erosion. The procedure is based on equations developed in section 3.4. The most recent meteorological data and the current geology of the study area were used as the starting point for the simulations. The procedure is summarized in the flowchart shown in Fig. 3.

The algorithm recognizes when a control volume belonging to the rock or soil is in contact with the air, i.e., a control volume at the ground surface that uses subscript *i_CV* in what follows. In our code a control volume is built with a rectangular parallelepiped, so the volume of soil corresponding to the initial volume of a superficial control volume (V_{in,i_CV}) is:

$$V_{wtr,i\_CV,t} \approx V_{in,i\_CV} = \Delta x_{i\_CV,t} \cdot \Delta y_{i\_CV,t} \cdot \Delta z_{i\_CV,t} \tag{21}$$

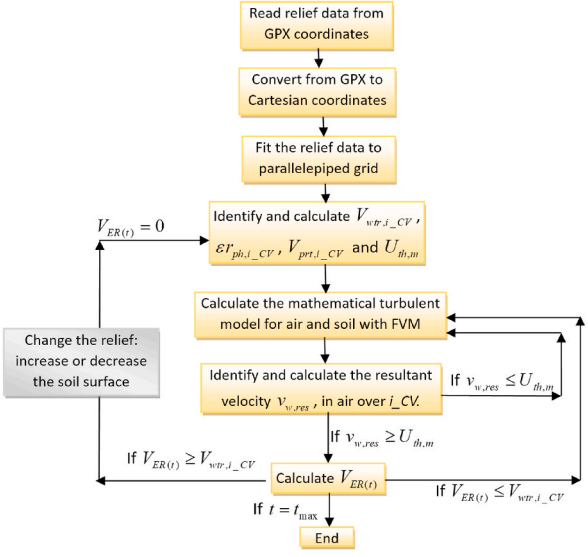

Fig. 3. Flowchart of the algorithm used to change the volume of soil due erosion.

Where $\Delta x_{i\_CV,t}, \Delta y_{i\_CV,t}$, and $\Delta z_{i\_CV,t}$ are the initial length of the *i-th* control volume (*i_CV*) at the ground surface in *x, y,* or *z* coordinates. This computational volume corresponds to the volume of the saprolite weathered soil ($V_{i\_CV,wtr}$). To calculate the volume of the fresh rock protolith, we first calculate the total volumetric strain ($\varepsilon r_{ph,i\_CV}$) using Eq. (15):

$$\varepsilon r_{ph,i\_CV} = \varepsilon r_{sum,i\_CV} = \frac{-(\tau m_{i\_CV} + 1)}{\psi_{wtr,i\_CV} - 1} - 1 \tag{22}$$

Note that the total volumetric strain in the previous equation considered the average precipitation and erosion rates as field data. This work assumed that the value of the mass transfer coefficient (τm_{i_CV}) is constant and unique for the study area. Using the result from Eq. (22) to obtain the volume of the *i_CV* corresponding to the fresh rock from Eq. (8) and with $\varepsilon r_{ch} = 0$, we have the following:

$$V_{prt,i\_CV} = \frac{V_{wtr,i\_CV}}{(\varepsilon r_{sum,i\_CV} + 1)} \tag{23}$$

To calculate the accumulated volume loss due to transport of soil particles, the following equation is used:

$$V_{ER(t)} = \sum_{t=t_0}^{t=t_{ER}} ER \cdot \Delta x_{i\_CV,t} \cdot \Delta z_{i\_CV,t} \tag{24}$$

where $V_{ER(t)}$ ($m^3\ yr^{-1}$) is the total volume lost during a simulation time (t_{ER}) for the *i_CV* as a function of the erosion rate (*ER*) observed in the field. Volume loss over time ($V_{ER(t)}$) only occurs if the turbulent air velocity ($v_{w,res}$) over the *i_CV* obtained from simulations is higher than the threshold velocity ($U_{th,m}$), i.e., $v_{w,res} \geq U_{th,m}$. In this work, the weathered material has the physical characteristics of sand, so Eq. (19) is used to calculate the threshold velocity. Finally, if the volume of the soil eroded $V_{ER(t)}$ exceeds the value calculated in Eq. (21) ($V_{ER(t)} \geq V_{wtr,i\_CV,t}$), the *i-CV* stops having properties of soil and begins to have properties of air.

Since erosion rate is considered to be constant, the above procedure can also be used to calculate the past relief of the study area. For this case, if the volume of the soil eroded $V_{ER(t)}$ exceeds the value calculated in Eq. (21) ($V_{ER(t)} \geq V_{wtr,i\_CV,t}$), the control volume over the *i_CV* (*y*-coordinate) stops having properties of air and begins to have properties of soil. When there is a volume change, $V_{ER(t)}$ returns to zero to start adding again.

Stress $S_{i,r,w}$ due to the wind force and Young's modulus for the *i_CV* can be calculated from Eqs. (12) and (13). Note that these parameters include the effects of the resultant air velocity at the ground surface exposed to air of the *i_CV* and of the moisture in the *i_CV*. Assuming isotropic behavior for the rock, Young's modulus is equal in all directions. The resulting volumetric strain due to the wind for the *i_CV* is:

$$\varepsilon r_{ph,w,i\_CV} = \frac{S_{r,w,i\_CV}}{\sigma_{r,i\_CV}} \tag{25}$$

Volumetric strain due to expansion and contraction from freezing and thawing of water in the rock resulting from snow, precipitation or relative humidity can be calculated for the *i_CV* as follows:

$$\varepsilon r_{ph,AAP,i\_CV} = \varepsilon r_{ph,i\_CV} - \varepsilon r_{ph,w,i\_CV} \tag{26}$$

5. Simulating erosion of a mudstone core in a wind tunnel

This section demonstrates how the proposed mathematical model and numerical algorithm accurately solves a case of rock erosion without volume changes. We solve the experimental setup presented in Ref. [13] for rocks in arid zones. The simulated physical situation uses a mudstone core placed in a cylindrical tunnel 1.55 m long and 0.42 m in diameter with a constant wind inlet velocity for 168 days. A flat layer was placed at the bottom of the tunnel reducing the effective diameter in the *y*-coordinate to 0.35 m. The cylindrical mudstone core was 0.054 m in diameter with a length/diameter ratio of 2.5 and total weight of 0.686 kg giving a density ρ_{app} = 2220 kg/m^3. The sample core was placed 0.2 m from the air inlet. Fig. 4 show the experimental physical situation.

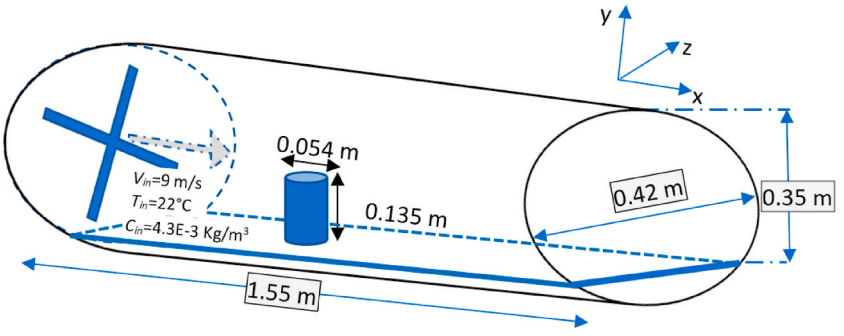

Fig. 4. Diagram of a mudstone rock exposed in a wind tunnel.

The average velocity of air over the rock core is measured experimentally and has a value of $V_{in} = 9$ m s^{-1}. A constant temperature of 22 °C for air and rock was assumed which means that the energy equation under isothermal conditions does not need to be calculated. The tunnel walls are considered impermeable. The effective diffusion coefficient varied between 6.5E-8 m^2 s^{-1} to 1.6E-7 m^2 s^{-1}. More details about the parameters used in the simulation can be consulted in the supplementary material.

Five different grids were tested to assure accuracy of the results and to validate the mathematical model. The grids tested are listed in Table 2. The grid is finer in the region occupied by the rock and nearby.

The relative error (*RE*) was calculated for each grid. The maximum relative error (RE_{max}) between calculated and experimental data is presented in Fig. 5A for each grid. The RE_{max} increases as the number of nodes decreases. A RE_{max} over 30 % was observed for grids 4 and 5. Grids 1 and 2 show a low RE_{max} of 2.0 % and 2.6 %, respectively, and good agreement with the experimental results; however, the computational time for grid 2 is about three times less than for grid 1.

The non-uniform grid 2 of 108 × 56 × 40 cells and a variable time step of 1s up to 30 min and 600s thereafter are suitable for reproducing experimental data with the numerical algorithm, so it was used for the simulations. Fig. 5a compares results from the numerical simulations with experimental data for water content evolution in the rock sample over 168 days. The moisture content decreases with the time. An increase of strain with weight lost is observed in Fig. 5b. Our calculated values are close to the experimental results obtained in Ref. [13]. Strain increases as humidity lost by the rock increases. In other words for this case, the external forces from the wind produce a bigger strain in dry rocks than in wet rocks. This behavior augments the weathering and erosion of rocks located in arid zones [8,9].

Fig. 6a shows that the highest velocities in the wind tunnel exceeding 9 m s^{-1} occur in the zone above the rock sample. A small vortex is generated in the upper part of the downstream side of the rock sample, which over time may cause weathering of the rock. Negative and low intensity velocities are observed in the upstream side of the rock sample indicating recirculation in the z-axis (not shown in this figure). Three-dimensional streamlines are shown in Fig. 6b. The lowest velocities are observed near the tunnel walls and floor, while the highest velocities are observed near the center of the tunnel. These results agree with those expected from the velocity boundary layer theory.

6. Simulation results for Fine Gold area

This section presents the numerical results for the Fine Gold area. They are based on the physical and environmental characteristics outlined in section 2 and the numerical considerations in section 4.1. The complete mathematical model of section 3 and computational procedure including volume changes of section 4.2 were applied. Computer codes, videos, and supplementary material used to obtain the results in this section can be downloaded from the following link: https://drive.google.com/drive/folders/1kqiNYx9QtUxGnTlrze5m18a0QQm_x5VA?usp=share_link.

Fig. 7 displays the 3D streamlines for the study area simulated at 150 ka into the future in the month of September. The colors of the streamlines indicate the magnitude of the *u*-velocity that varies between −0.1 m s^{-1} and 3.3 m s^{-1}. This figure also includes a *y*-*z* plane at $x = 1500$ m colored with *u*-velocity contours. The wind source is in the southeast, as assumed for the programmed boundary conditions in Eq. (7). The lowest velocities are closest to the ground while the highest are the furthest away. Areas of low velocity and even recirculation occur near the steepest elevation changes. In general, the streamlines and velocities were very similar for simulations 150 ka into the past before changes in relief occurred.

Fig. 8 shows the wind velocity, water content, temperature, and turbulent kinetic energy production (κ) in the *x*-*y* plane at $z = 1320$ m simulated 150 ka into the future for the month of September. As mentioned in the introduction, the effects of turbulence in the ABL were included by using RANS equations to which a turbulent viscosity or eddy model was applied to calculate the Reynolds stresses. Similarly, turbulent thermal and mass diffusivities for heat and air moisture were used for the turbulent diffusion equations. Therefore, these statistical means are the only kinematic variables that can be solved explicitly using a RANS computation. As a result, although the calculation is unstable, the snapshot shown in Fig. 8 represents only the instantaneous mean flow, since the turbulent fluctuations have been grouped into the Reynolds stresses and their effects have been introduced through the turbulence model. As part of the ABL, a layer closer to the ground called the Atmospheric Surface Layer (ASL) makes up 10 % of the thickness of the ABL. The complex surface relief produces distortions in the atmospheric flow which are controlled by the local conditions of the boundary layer. In those zones, we apply wall functions that allow us to introduce these effects in the $\kappa-\varepsilon$ equations in near-wall regions. (See the mathematical model in the supplementary material.)

Fig. 8a shows that the streamlines are modified by the ground relief. The highest *u*-velocities between 2 and 2.5 m s^{-1} are observed

Table 2
Grids tested to compare calculated results with experimental data.

Grid	x nodes	y nodes	z nodes	Total nodes
1	134	69	50	462300
2	108	56	40	241920
3	84	44	32	118272
4	67	35	24	56280
5	54	28	20	30240

Grid convergence was assessed by comparing our results with experimental data from Ref. [13]. The comparison included calculated moisture content and experimental data for moisture at different times.

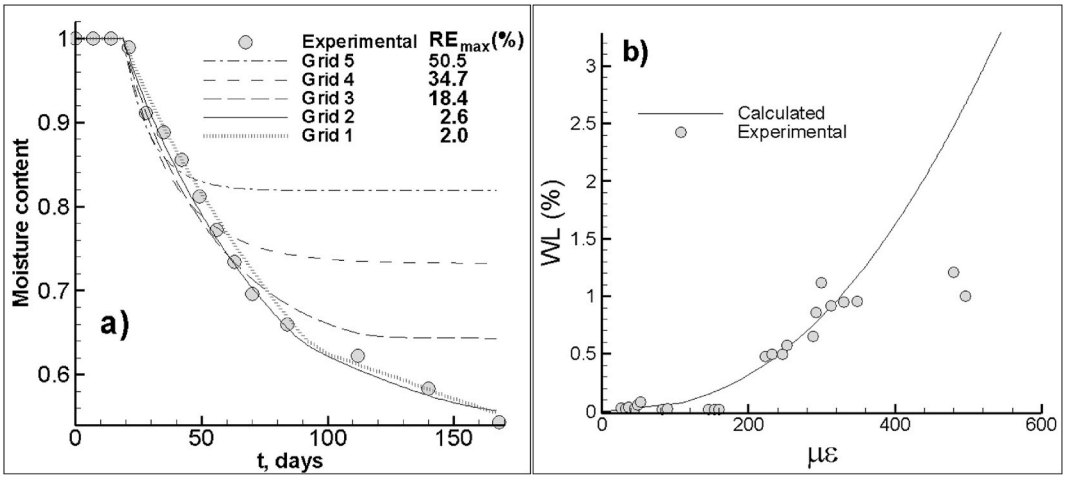

Fig. 5. Comparison between experimental and calculated results for a mudstone sample located in a wind tunnel for 168 days. The comparison is for: a) a decrease in moisture content with time and b) an increase in strain (micro strain, $\mu\varepsilon$) with moisture lost. Experimental data were obtained from Ref. [13].

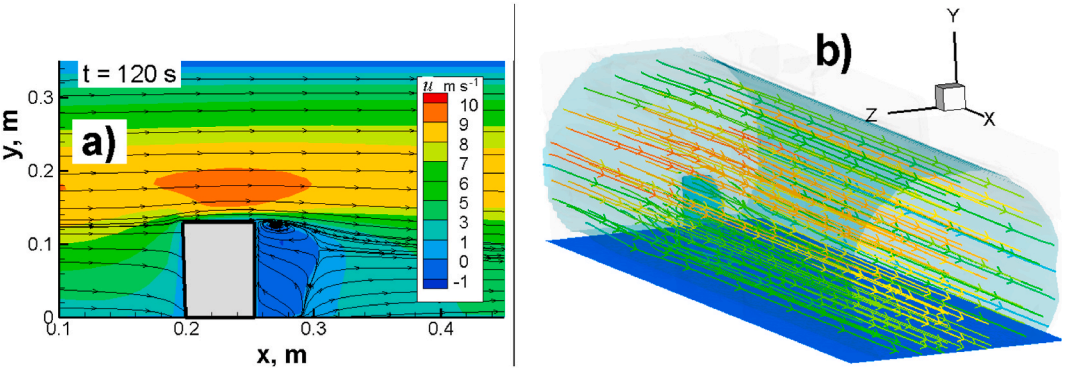

Fig. 6. a) Streamlines in black and u air velocities in colored contours for the mid-plain (z = 0.21 m) of the wind tunnel. b) Three-dimensional stream lines colored with u air velocities contours inside the wind tunnel and around the rock sample. Both figures were obtained after 120 s of simulation. The streamlines and velocities remain unchanged after that time.

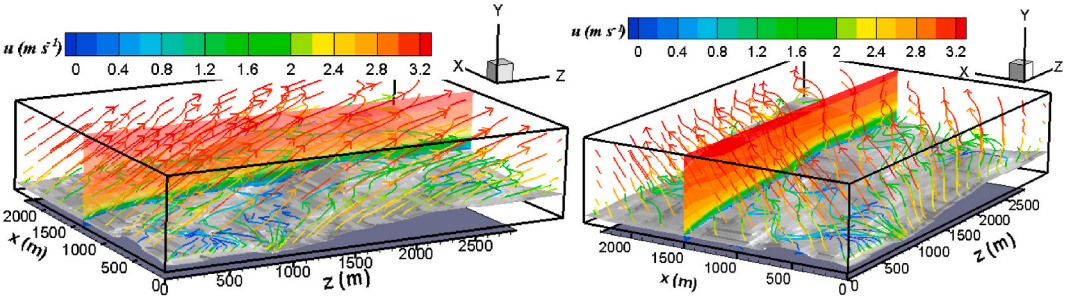

Fig. 7. Wind velocities simulated for 150 ka into the future as viewed from two different angles over the Fine Gold study area. The u-velocities are shown as 3D streamlines and as contours on the y-z plane at x = 1500 m. In this figure, the x and z coordinates are related to the south-north (S–N) and west-east (W–E) geographic directions, respectively while the y-coordinate is related to meters above sea level (masl) (see Fig. 1). (For interpretation of the references to color in this figure legend, the reader is referred to the Web version of this article.)

at high elevations far from the ground surface. The lowest u-velocities at ground level are around of 0.5 m s^{-1}.

Fig. 8b shows that the water content in the air is due to the average relative humidity and the rainfall for the month of 0.014. At greater than 30 m of depth from the surface, fresh tonalite rock has an assumed water content of 0.01 as noted in section 3.3. Land areas

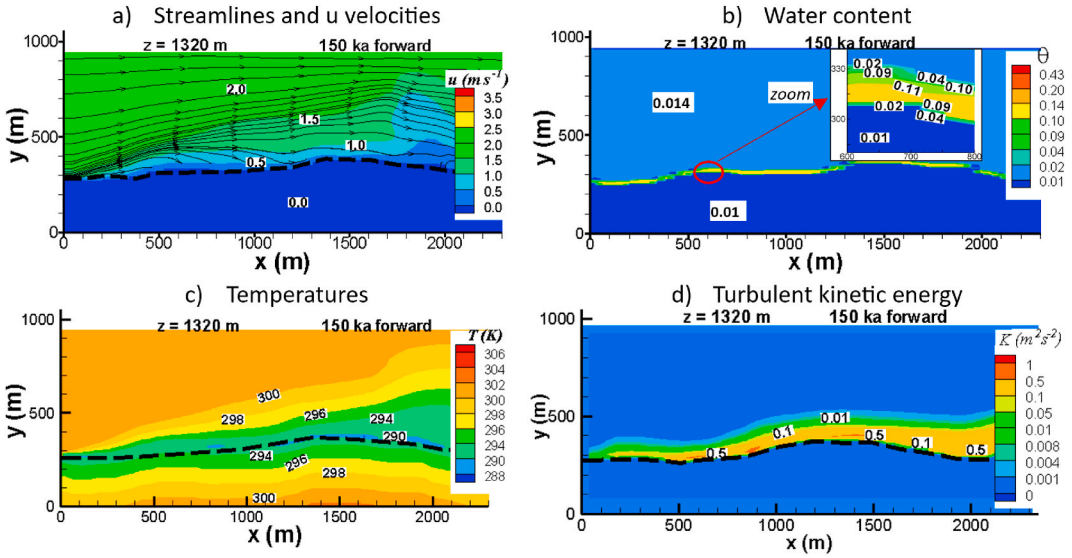

Fig. 8. Values calculated 150 ka into the future on the x (S–N direction) and y (masl) plane at $z = 1320$ m for: a) streamlines and u-velocities, b) water content, c) temperatures in Kelvin, and d) turbulent kinetic energy. The heavy dashed line is approximately the location of the ground surface at $z = 1320$ m.

with low inclination or between two slopes with opposite inclinations would be expected to have a greater quantity of atmospheric water that comes from humid air and rain. The simulations reproduced these expectations showing higher water content in areas with less slope and less water content in areas with a greater slope. The inset for Fig. 8b shows the water distribution at a promontory 30 m down into the soil and 10 m up into the air. At approximately 15 m depth, the water content has a maximum value of 0.11. Water content in the air is between 0.014 and 0.02. Because air velocity and humidity are not uniform over the ground surface, erosion and change in soil relief is not uniform either. This work includes the drag of soil particles only if air velocity over the ground surface exceeds the threshold velocity of Eq. (19). For the moisture conditions observed at the earth's surface in Fig. 8b, the threshold velocity is below 0.5 because the water content is lower than 0.04, and therefore the ground is eroding.

Fig. 8c shows how temperature contours generated by heat from the Earth's interior are not altered by air temperatures near Earth's surface. In our simulations the air temperature input is the monthly average temperature value and not a temperature profile. This was done in order to observe the effect of soil temperature on air temperature, and if possible, develop a temperature profile across the study area. The air temperature at the ground surface is 10 °C lower than the average temperature of 28 °C or 301 K in the area for September.

As expected, the turbulent kinetic energy (κ) in Fig. 8d is greatest near the ground surface and lower further away. The highest

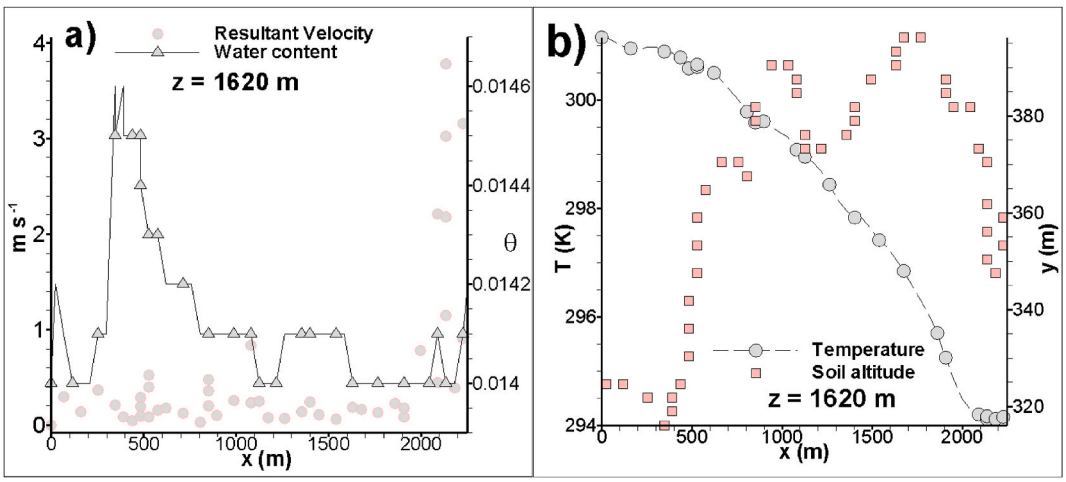

Fig. 9. Profiles for control volumes at the soil surface calculated 150 ka forward in time for the month of September. Profiles are along the x-coordinate showing the soil surface altitude in the y-coordinate approximately midway along the z-axis at $z = 1620$ m. Profiles are for: a) resultant velocity and water content and b) temperature and soil altitude.

values range from 0.5 to 1 $m^2\ s^{-2}$, and when approaching 1 $m^2\ s^{-2}$ are associated with abrupt changes in relief. These values predict greater turbulence at the ground surface which means a greater production of instabilities or vortices, higher local wind velocities at the ground surface, and more erosion.

Fig. 9 shows profiles along the x-coordinate at the (y-coordinate) soil surface and z = 1620 m for velocity, water content, and temperature in the air above ground. The velocity in Fig. 9a remains below 1 m s^{-1} until $x = 2000$ m where it increases to about 4 m s^{-1} due to an abrupt change in altitude shown in Fig. 9b. The water content in Fig. 9a varies slightly between 0.014 and 0.0146 with the highest value where a sharp elevation change occurs as shown in Fig. 9b.

Fig. 9b shows the steady decrease in temperature from the inlet temperature of 301 K in September to approximately the soil temperature of 294 K. Fig. 9 shows that the relief of the ground surface affects wind velocity and water content of the air, but not the air temperature.

Fig. 10 shows an aerial view of the Fine Gold study area with an x-z plane at three simulation times: the present, 150 ka forward in time, and 150 ka back in time. The figure shows the change in relief with time. The difference between cases is that the y-coordinate for the soil surface decreases in the future and increases in the past. This occurs if the cumulative lost volume in Eq. (24) due to the accumulated erosion exceeds the computational control volume. The plane from the satellite image in Fig. 5 and the one adjusted to the computational grid in Fig. 10a agree as to the elevation and location of the relief.

Fig. 10b simulates the results of erosion by wind, temperature, and humidity including precipitation over time. Decrease in relief elevation does not occur over the entire area because in some areas the threshold wind velocity is not exceeded, so particle transport does not occur. The threshold wind velocity obtained with Eq. (19) varies between 1.5 and 0.34 m s^{-1}. The greatest erosion occurs in areas where the relief increases sharply, because the wind velocities are higher as seen in Figs. 8 and 9. In flat areas, the soil accumulates a higher water content, as can be seen in Fig. 8b, causing an increase in the threshold velocity and therefore decreasing erosion. Fig. 10c displays a similar analysis for soil relief, but simulates 150 ka back in time. The result is that higher elevation areas cover a larger domain than in Fig. 10a.

Fig. 11 displays values for deformation of rock in contact with air: at the surface due to wind and in the interior due to freezing and thawing of the water. The profile in the x-coordinate is midway on the z-axis at $z = 1425$ m. Total volumetric strain calculated from Eqs. (15) and (22) is 0.475. Strain due to wind is very low at less than 0.0145 and varies slightly due to ground relief. Strain due to freezing and thawing of water varies from 0.461 to 0.475, and hence is the volumetric strain that contributes most to weathering of the rock.

7. Limitations and future direction of this study

As mentioned in the introduction, this study is only limited to the erosion of soils formed from intrusive rocks with sparse vegetation and does not consider landslides, channeling or displacement of water, long-term geological processes or chemical weathering. Each of these topics involves the development and/or incorporation of new mathematical models and computational algorithms which can be addressed in future work.

Computational simulation of large areas is limited by the type and size of control volumes that can be processed. In our simulation of the Fine Gold site, a non-uniform parallelepiped grid of about 3 million control volumes was used, which was constructed denser at the soil-air interface. Even so, the minimum height that was achieved in a control volume of this interface was 2.86 m, which is not enough to capture the relief accurately, especially in more abrupt areas. This could affect the accuracy of the results. So from the computational point of view it is possible to improve the type and size of the control volumes. In future works, the current grid with parallelepipeds could be changed to one where the control volumes adhere better to the relief and parallelize the calculation algorithm to increase the number of control volumes and decrease the calculation times.

8. Conclusions

A mathematical model and three-dimensional computer simulations have been developed to predict the change in soil relief due to erosion. The computations use an algorithm to fit GPX coordinates from satellite images to a computational grid. This allows the discretization of space-time and the calculation of variables using the finite volume numerical method. The simulations include environmental variables for air that flows over the soil surface: temperature, turbulent air, and humid air that incorporates both relative air humidity and precipitation. Simulations also include water content and temperature variations in the soil.

Application to erosion of a mudstone core, without volume change, verified the proposed model. Simulations reproduced the experimental data for water loss in the mudstone core with good precision and the variation in strain due to water content.

The computational simulations were applied to the Fine Gold area in the Sierra Nevada Mountains of California and predicted the change in soil relief due to erosion after 150 ka. Moisture from humid air and precipitation infiltrates flat areas, but is limited to the first 30 m of depth since fresh rock is found below that. Ambient air temperatures are not observed to affect soil temperature.

Wind velocity is higher in areas where the relief changes rapidly. Erosion especially occurs in these areas, since the threshold wind velocity for particle transport of weathered soil is exceeded.

The physical strain produced by air on the rock is a small part of the total strain. The greatest deformation results from expansion and contraction due to freezing and thawing of the water contained in the rock.

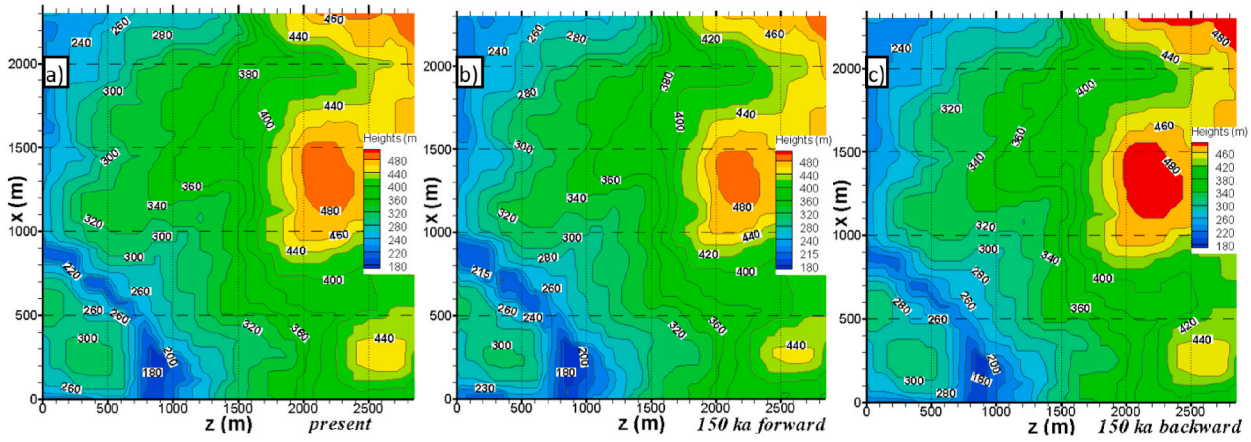

Fig. 10. The x-z relief plane for the Fine Gold area: a) at present, b) for simulations 150 ka forward in time, and c) 150 ka back in time. (For interpretation of the references to color in this figure legend, the reader is referred to the Web version of this article.)

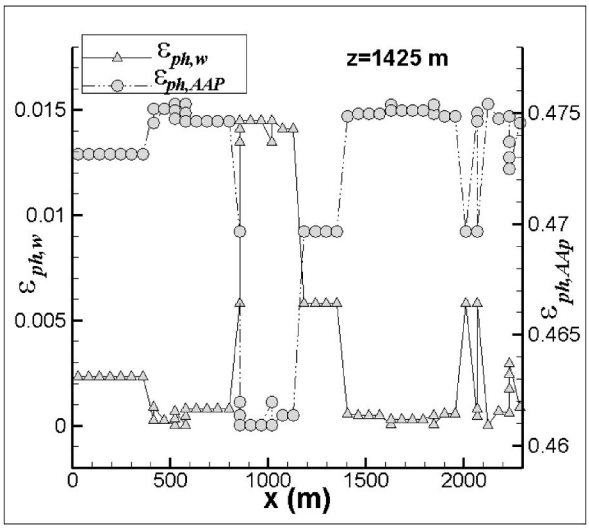

Fig. 11. Physical strain values of the rock due to wind $\varepsilon r_{ph,w}$ and the freezing and thawing of water $\varepsilon r_{ph,AAP}$. The x-profile was obtained at z = 1425 m and for January atmospheric conditions.

Data availability statement

The FORTRAN code, supplementary material and videos can be downloaded from https://drive.google.com/drive/folders/1kqiNYx9QtUxGnTlrze5m18a0QQm_x5VA?usp=share_link.

CRediT authorship contribution statement

Carlos Zambra: Writing – review & editing, Writing – original draft, Visualization, Validation, Software, Methodology, Investigation, Formal analysis, Conceptualization. **Benjamin Clausen:** Writing – review & editing, Project administration, Funding acquisition, Formal analysis. **Diego Vasco:** Writing – review & editing, Formal analysis. **Roberto Lemus-Mondaca:** Writing – review & editing, Formal analysis.

Funding statement

The authors thank the Geoscience Research Institute at Loma Linda University for supporting this research.

Declaration of competing interest

The authors declare that they have no known competing financial interests or personal relationships that could have appeared to influence the work reported in this paper.

Appendix A. Supplementary data

Supplementary data to this article can be found online at https://doi.org/10.1016/j.heliyon.2023.e21044.

References

[1] A. Balasubramanian, Soil Forming Processes: Technical Report, 2017, https://doi.org/10.13140/RG.2.2.34636.00644.
[2] Y. Israeli, S. Emmanuel, Impact of grain size and rock composition on simulated rock weathering, Earth Surf. Dyn. 6 (2018) 319–327, https://doi.org/10.5194/esurf-6-319-2018.
[3] X. Wang, Y. Tang, B. Huang, T. Hu, D. Ling, Review on numerical simulation of the internal soil erosion mechanisms using the discrete element method, Water (Switzerland) 13 (2021) 1–17, https://doi.org/10.3390/w13020169.
[4] D. Aringoli, M. Calista, B. Gentili, G. Pambianchi, N. Sciarra, Geomorphological features and 3D modelling of Montelparo mass movement (Central Italy), Eng. Geol. 99 (2008) 70–84, https://doi.org/10.1016/j.enggeo.2007.11.005.
[5] Y. Ye, X. Tan, C. Zhou, Initial topography matters in drainage divide migration analysis: insights from numerical simulations and natural examples, Geomorphology 409 (2022), 108266, https://doi.org/10.1016/j.geomorph.2022.108266.
[6] C.S. Riebe, W.J. Hahm, S.L. Brantley, Controls on deep critical zone architecture: a historical review and four testable hypotheses, Earth Surf. Process. Landforms 42 (2017) 128–156, https://doi.org/10.1002/esp.4052.
[7] M.I. Lebedeva, R.C. Fletcher, V.N. Balashov, S.L. Brantley, A reactive diffusion model describing transformation of bedrock to saprolite, Chem. Geol. 244 (2007) 624–645, https://doi.org/10.1016/j.chemgeo.2007.07.008.
[8] C.S. Riebe, R.P. Callahan, S.B.M. Granke, B.J. Carr, J.L. Hayes, M.S. Schell, L.S. Sklar, Anisovolumetric weathering in granitic saprolite controlled by climate and erosion rate, Geology 49 (2021) 551–555, https://doi.org/10.1130/G48191.1551-555.
[9] J.L. Hayes, C.S. Riebe, W. Steven Holbrook, B.A. Flinchum, P.C. Hartsough, Porosity production in weathered rock: where volumetric strain dominates over chemical mass loss, Sci. Adv. 5 (2019) 1–12, https://doi.org/10.1126/sciadv.aao0834.
[10] A. Rohrmann, R. Heermance, P. Kapp, F. Cai, Wind as the primary driver of erosion in the qaidam basin, China, earth planet, Sci. Lett. 374 (2013) 1–10, https://doi.org/10.1016/j.epsl.2013.03.011.
[11] N. Dannhaus, H. Wittmann, P. Krám, M. Christl, F. von Blanckenburg, Catchment-wide weathering and erosion rates of mafic, ultramafic, and granitic rock from cosmogenic meteoric 10Be/9Be ratios, Geochim. Cosmochim. Acta. 222 (2018) 618–641, https://doi.org/10.1016/j.gca.2017.11.005.
[12] N.D. Brown, S. Moon, Revisiting erosion rate estimates from luminescence profiles in exposed bedrock surfaces using stochastic erosion simulations, Earth Planet Sci. Lett. 528 (2019), 115842, https://doi.org/10.1016/j.epsl.2019.115842.
[13] A. Binal, The effect of wind pressure on surface erosion of soft rocks in arid regions, Bull. Eng. Geol. Environ. 78 (2019) 1565–1574, https://doi.org/10.1007/s10064-017-1218-x.
[14] P. Borrelli, C. Alewell, P. Alvarez, J.A.A. Anache, J. Baartman, C. Ballabio, N. Bezak, M. Biddoccu, A. Cerdà, D. Chalise, S. Chen, W. Chen, A.M. De Girolamo, G. D. Gessesse, D. Deumlich, N. Diodato, N. Efthimiou, G. Erpul, P. Fiener, M. Freppaz, F. Gentile, A. Gericke, N. Haregeweyn, B. Hu, A. Jeanneau, K. Kaffas, M. Kiani-Harchegani, I.L. Villuendas, C. Li, L. Lombardo, M. López-Vicente, M.E. Lucas-Borja, M. Märker, F. Matthews, C. Miao, M. Mikoš, S. Modugno, M. Möller, V. Naipal, M. Nearing, S. Owusu, D. Panday, E. Patault, C.V. Patriche, L. Poggio, R. Portes, L. Quijano, M.R. Rahdari, M. Renima, G.F. Ricci, J. Rodrigo-Comino, S. Saia, A.N. Samani, C. Schillaci, V. Syrris, H.S. Kim, D.N. Spinola, P.T. Oliveira, H. Teng, R. Thapa, K. Vantas, D. Vieira, J.E. Yang, S. Yin, D. A. Zema, G. Zhao, P. Panagos, Soil erosion modelling: a global review and statistical analysis, Sci. Total Environ. 780 (2021), https://doi.org/10.1016/j.scitotenv.2021.146494.
[15] J.P. de Lima Costa Salazar, R. Albani, Atmospheric boundary layer flow simulations with OpenFOAM using a modified k-epsilon model consistent with prescribed inlet conditions, 13th Spring Sch. Transit. Turbul. (2022), https://doi.org/10.26678/abcm.eptt2022.ept22-0081.
[16] S. Kenjereš, K. Hanjalić, Tackling complex turbulent flows with transient RANS, Fluid Dyn. Res. 41 (2009), https://doi.org/10.1088/0169-5983/41/1/012201.
[17] M. Shirzadi, P.A. Mirzaei, M. Naghashzadegan, Improvement of k-epsilon turbulence model for CFD simulation of atmospheric boundary layer around a high-rise building using stochastic optimization and Monte Carlo Sampling technique, J. Wind Eng. Ind. Aerodyn. 171 (2017) 366–379, https://doi.org/10.1016/j.jweia.2017.10.005.
[18] M.P. Van Der Laan, M. Kelly, M. Baungaard, A pressure-driven atmospheric boundary layer model satisfying Rossby and Reynolds number similarity, Wind Energy Sci 6 (2021) 777–790, https://doi.org/10.5194/wes-6-777-2021.
[19] K. Al-mashrafi, Diffusion of dust particles emitted from a fixed source, Int. J. Appl. Math. Res. 4 (2015) 454, https://doi.org/10.14419/ijamr.v4i4.5058.
[20] Z. Dong, X. Liu, X. Wang, Wind initiation thresholds of the moistened sands, Geophys. Res. Lett. 29 (2002), https://doi.org/10.1029/2001GL013128, 25-1-25–4.
[21] P.C. Bateman, Plutonism in the Central Part of the Sierra Nevada Batholith, California, 1992, https://doi.org/10.3133/pp1483.
[22] A.R. Gillespie, P.H. Zehfuss, Glaciations of the sierra Nevada, California, USA, in: J. Ehlers, P.L. Gibbard, A.R. Gillespie, P.H. Zehfuss (Eds.), Quatemary Glaciat. Chronol. Part II North Am. Dev. Quat. Sci., vol. 2b, Elsevier Amsterdam, 2004, pp. 51–62.
[23] WeatherWX.com, WeatherWX_com_meteorologia, Millert. Lake, Calif. Clim. Aver (2022) 1. https://www.weatherwx.com/climate-averages/ca/millerton+lake.html. (Accessed 19 December 2022).
[24] R. Lemus-Mondaca, C. Zambra, C. Rosales, Computational modelling and energy consumption of turbulent 3D drying process of olive-waste cake, J. Food Eng. 263 (2019), https://doi.org/10.1016/j.jfoodeng.2019.05.036.
[25] H.M. Veersteg, W. Malalasekera, An Introductionto Computational Fluid Dynamic: the Finite Volume Method, Second, Harlow, 2007.
[26] A. Castro, Tonalite-granodiorite suites as cotectic systems: a review of experimental studies with applications to granitoid petrogenesis, Earth-Science Rev. 124 (2013) 68–95, https://doi.org/10.1016/j.earscirev.2013.05.006.
[27] C.E. Zambra, N.O. Moraga, M. Escudey, Heat and mass transfer in unsaturated porous media: moisture effects in compost piles self-heating, Int. J. Heat Mass Transf. 54 (2011) 2801–2810, https://doi.org/10.1016/j.ijheatmasstransfer.2011.01.031.
[28] J. González, C.E. Zambra, L. González, B. Clausen, D.A. Vasco, Geothermics Simulation of cooling in a magma chamber : implications for geothermal fields of southern Peru, Geothermics 105 (2022), https://doi.org/10.1016/j.geothermics.2022.102515.
[29] M. Schneebeli, H. Flühler, T. Gimmi, H. Wydler, H.-P. Läser, T. Baer, Measurements of water potential and water content in unsaturated cystalline rock, Water Resour. Res. 31 (1995) 1837–1843, https://doi.org/10.1029/95WR01487.
[30] S. Patankar, Numerical Heat Transfer and Fluid Flow: Computational Methods in Mechanics and Thermal Science, 1980.
[31] S.V. Patankar, Computational of Conduction and Duct Flow Heat Transfer, CRC Taylor & Francis Group, 1991.

[32] C.E. Zambra, L. Puente-Díaz, K. Ah-Hen, C. Rosales, D. Hernandez, R. Lemus-Mondaca, Experimental and numerical study of a turbulent air-drying process for an ellipsoidal fruit with volume changes, Foods 11 (1880) (2022), https://doi.org/10.3390/foods11131880.
[33] C.E. Zambra, N.O. Moraga, C. Rosales, E. Lictevout, Unsteady 3D heat and mass transfer diffusion coupled with turbulent forced convection for compost piles with chemical and biological reactions, Int. J. Heat Mass Transf. 55 (2012) 6695–6704, https://doi.org/10.1016/j.ijheatmasstransfer.2012.06.078.
[34] X.M. Hu, Boundary layer (atmospheric) and air pollution: air pollution meteorology, Encycl. Atmos. Sci. Second Ed. 1 (2015) 227–236, https://doi.org/10.1016/B978-0-12-382225-3.00499-0.